Comparative Study on Wire-Arc Additive Manufacturing and Conventional Casting of Al–Si Alloys: Porosity, Microstructure and Mechanical Property

Yueling Guo[1] · Qifei Han[2] · Jinlong Hu[2] · Xinghai Yang[2] · Pengcheng Mao[3] · Junsheng Wang[2,4] · Shaobo Sun[5] · Zhi He[5] · Jiping Lu[1] · Changmeng Liu[1]

Abstract

Here, we compare the porosity, microstructure and mechanical property of 4047 Al–Si alloys prepared by wire-arc additive manufacturing (WAAM) and conventional casting. X-ray microscopy reveals that WAAM causes a higher volume fraction of gas pores in comparison with conventional casting. Effective refinements of α-Al dendrites, eutectic Si particles and Fe-rich intermetallic compounds are achieved by WAAM, resulting from its rapid solidification process. Both ultimate tensile strength (UTS, up to 205.6 MPa) and yield stress (YS, up to 98.0 MPa) are improved by WAAM at the expense of elongation after fracture. The mechanical property anisotropy between scanning direction and build direction is minimal for alloys via WAAM. Additional microstructure refinement and strength enhancement are enabled by increasing the travel speed of welding torch from 300 to 420 mm/min.

Keywords Wire-arc additive manufacturing · Al–Si alloy · Porosity · Microstructure · Strength

1 Introduction

Wire-arc additive manufacturing (WAAM) has drawn extensive attentions due to its ability to fabricate large-scale near-net components in a low-cost and high-efficiency way [1, 2]. High-energy electric arc works as the heat source using wires as the feedstock, generating a similar metallurgical process as fusion welding [3]. Considering the widespread structural applications of aluminum alloys in key sectors like weapons, transportation, aerospace, etc., it is thus of theoretical and practical importance to explore their WAAM processing feasibility and mechanical properties.

Metallurgical defect and microstructure are the two primary factors that determine the mechanical property of WAAM-processed aluminum alloys [2, 3]. Hydrogen porosity is a notorious metallurgical defect of aluminum alloys via not only additive manufacturing but also welding and conventional casting, which severely deteriorates the alloys' mechanical properties [4–7]. WAAM processing parameter optimization is the commonly used method to reduce porosity, including travel speed [2], arc current [8], etc., together with the controlling of surface quality and warpage of wires [9]. Such measures are taken to both minimize hydrogen absorption during fusion and maximize gas escaping during solidification that involves a combined effect of chemical reacts, curvature radius and liquid viscosity [8, 10]. The maturation of cold metal transfer (CMT) welding, featured by a short-circuiting transfer process, has been verified as an effective pathway to eliminate porosity defects [11–13].

The rapid solidification process of WAAM normally results in a significant microstructural refinement,

✉ Yueling Guo
   y.guo@bit.edu.cn

✉ Changmeng Liu
   liuchangmeng@bit.edu.cn

1   School of Mechanical Engineering, Beijing Institute of Technology, Beijing 100081, China

2   School of Materials Science and Engineering, Beijing Institute of Technology, Beijing 100081, China

3   Center for Micro and Nano Technologies, Beijing Institute of Technology, Beijing 100081, China

4   Advanced Research Institute of Multidisciplinary Science, Beijing Institute of Technology, Beijing 100081, China

5   Beijing Hangxing Machinery Manufacturing Co., Ltd,, Beijing 100013, China

non-equilibrium phase growth and unique microstructures associated with the layer-wise deposition. Zhou et al. [2] report that for the WAAM-processed 2219 alloy, each deposited layer forms the inner-layer region consisting of coarse columnar grains and the inter-layer region composed of equiaxed grains. Increasing the travel speed of welding torch contributes to a reduced inter-layer size and a lower volume fraction of equiaxed grains, as well as more θ phase precipitates [2]. Miao et al. [14] find that coarse discrete Si particles are produced within the heat-affected zone, i.e., the melt pool boundary, which have a lower hardness and act as the preferred crack propagation routes under mechanical loading.

The joint effects of metallurgical defect and microstructure should be defined in a specific alloy system. Attempts of WAAM processing have been performed on wrought (Al–Cu, Al–Mg, Al–Zn–Cu–Mg, etc.) [2, 11, 15–17] and cast (Al–Si, etc.) [14, 18] aluminum alloys. It is not surprising to find that in comparison with wrought alloys, cast aluminum alloys are more suitable for the solidification-based processing routine of WAAM. Haselhuhn et al. [19] state that 4000 series (Al–Si) alloys show better performances than the 1100 and 5356 alloys in terms of porosity, strength and defect sensitivity. However, Al–Si alloys have well-developed and widely used industrial casting routes, which makes WAAM probably less attractive. A comparative study on the mechanical performances of Al–Si alloys via either conventional casting or WAAM is thus of importance to manifest whether WAAM is promising for Al–Si alloys.

In this work, the 4047 Al–Si alloy, with the Si content up to 11.5 wt%, is processed by WAAM, considering its narrow solidification temperature range (565–575 °C) and thus low crack sensitivity [20]. Also, the counterpart alloy via conventional casting is prepared for comparison. Porosity characterization, microstructure analysis and mechanical property testing are performed to investigate their differences in structure–property relationship. Useful guidance for industrial applications is thus provided for the WAAM processing of Al–Si alloys, which is distinguished by both strength improvement and manufacturing advantages.

2 Experimental

The SAL4047 welding wires, 1.2 mm in diameter, were used to fabricate the experimental Al–Si alloys, and the composition is listed in Table 1. The WAAM equipment utilized in this work was mainly composed of a welding machine (Fronius CMT Advanced 4000 R), a six-axis industrial robot manipulator (FANUC M710iC-50) for positioning, a controlling system and a steel sheet platform. This steel platform was used to not only support and fix the aluminum substrate, but also to facilitate rapid heat dissipation generated during WAAM. The CMT pulse (CMT-P) mode was employed for WAAM processing. The average current value was 113 A, and the feeding speed of SAL4047 wires was 5.5 m/min. The argon shielding gas flow rate was 22 L/min. Two thin walls with a respective welding torch traveling speed of 300 mm/min and 420 mm/min were prepared, denoted as AM300 and AM420, respectively. The process of WAAM is portrayed in Fig. 1a. For a comparative investigation, the cast counterpart alloy was prepared by a vacuum-argon pressure casting machine with a graphite crucible, using SAL4047 wires as raw materials. Sampling positions for microstructure analysis and tensile testing are illustrated in Fig. 1b.

X-ray diffraction (XRD, Cu-$K\alpha$ radiation, Rigaku Smart-Lab-SE, Japan) was performed to determine the phase constitution with a scanning rate of 5°/min. Samples for

Table 1 Chemical composition of SAL4047 welding wire measured using a direct reading spectrometer (wt%)

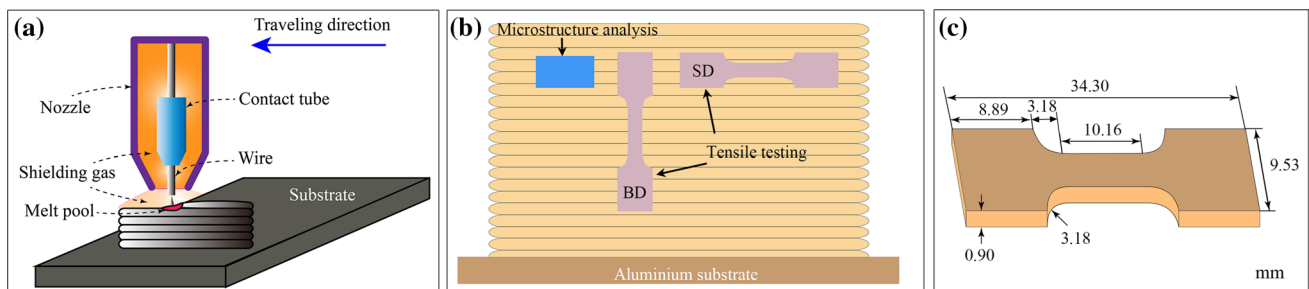| Element	Al	Si	Fe	Cu	Mn	Mg	Zn	Ti
Nominal range	Bal.	11.0–13.0	<0.60	<0.30	<0.15	<0.10	<0.20	<0.15
Measured	Bal.	11.5	0.543	0.023	0.098	0.085	0.120	0.075

Fig. 1 **a** Schematic illustration of cold metal transfer (CMT)-based WAAM; **b** sampling positions for microstructure analysis and mechanical testing along building direction (BD) and scanning direction (SD); **c** specimen dimensions for tensile testing

microstructural observation were prepared according to the standard grinding and polishing procedures with a final OPS polishing. Microstructures were firstly observed using an inverted optical metallographic microscope (LWD200-4XC) and then analyzed by a scanning electron microscope (SEM, JSM-7001F) attached with an energy-dispersive X-ray spectrometer (EDS). Secondary dendrite arm spacing (SDAS), the length parallel to the primary arm from two adjacent secondary arm centers, was measured using optical images. For each alloy, at least three images were used, with more than twenty SDAS measurements for each image.

X-ray microscopy (XRM, ZEISS Xradia 520 Versa), a non-destructive technique to image and quantify the three-dimensional microstructure at sub-micrometer length scale, was employed to investigate the porosity of WAAM-processed Al–Si alloys. Dog-bone specimens prepared for tensile testing were used for XRM analysis, and the corresponding specimen dimensions are illustrated in Fig. 1c. The gauge sections of representative dog-bone specimens were scanned by XRM, and the corresponding settings for each specimen were 60 kV beam voltage, 5 W beam power, 83 µA target current, 4X optical magnification, 1 s exposure time and 3.1 µm pixel size. A LE4 filter was utilized for enhancing X-ray transmission through the tested specimen. The XRM datasets were reconstructed and visualized using the Dragonfly Pro software.

Tensile testing was performed using a CMT4105 universal testing machine (Shenzhen XinSanSi Co., Ltd, China) at room temperature with a constant loading speed of 1 mm/min. The yield limit at 0.2% plastic strain was determined using a 5 mm gauge length extensometer. At least three specimens were tested for each alloy. After mechanical testing, the fracture surfaces were observed using a SEM (Zeiss Super 55).

3 Results

3.1 Microstructure Analysis

The Al–Si alloy thin walls prepared by WAAM with different welding torch travel speeds are displayed in Fig. 2, including the front and sectional views. The arcuate fusion lines, i.e., the melt pool boundaries, are observed on the sectional images. With the travel speed increasing from 300 to 420 mm/min, the average thin wall width decreases from 1.22 to 1.06 mm, suggesting a reduction of melt pool size. Figure 3 shows the optical microstructures of AM300 and AM420 alloys within melt pools, together with the cast alloy. Such alloys form hypoeutectic microstructures with primary α-Al dendrites and interdendritic eutectics, as the Si content (11.5 wt%) in the SAL4047 wire is lower than the eutectic composition of Al–Si binary system (12.2 wt%) [21].

The α-Al dendrites in AM300 and AM420 alloys exhibit a directional growth feature, which is correlated with the radial heat flow across melt pools [22]. In contrast, the α-Al dendrites in the cast alloy grow in random orientations. To quantitatively describe the microstructural length scale, the SDAS value of each experimental alloy is measured, as displayed in Fig. 3d. Evidently, the SDAS value of the cast alloy is much larger than that of the WAAM-processed alloys. Namely, WAAM enables significant microstructure refinement of Al–Si alloys. In addition, there is a tendency that a higher travel speed of the welding torch results in a finer SDAS. According to Fig. 3e, both WAAM-processed and conventional cast Al–Si alloys are composed α-Al and Si phases. This gives the evidence that the phase regime is not altered by the solidification process of WAAM, even with a wide travel speed range of welding torch from 300 to 420 mm/min.

The generation of melt pools is a major difference between WAAM and conventional casting, forming a number of periodically overlapped melt pool boundaries. Microstructures of the melt pool boundary zones in the WAAM-processed alloys and the cast alloy are imaged in Fig. 4. For the alloys via WAAM, there is a tendency that the increase in the travel speed of welding torch leads to a thinner melt pool boundary, from ~58.1 to ~13.9 µm. So is the eutectic Si particle size in melt pool boundary, decreasing from ~3.3 to ~0.9 µm, with the travel speed increasing from 300 to 420 mm/min. A coarser microstructure is observed at the melt pool boundaries, which is not uncommon for additive-manufactured alloys [14, 23]. The presence of large bulk Si particles is found at the melt pool boundaries, while lamellar or fibrous eutectic Si phases are noted within melt pools. This suggests a possible divorced growth mode of non-faceted α-Al and faceted Si that grow independently without mutual constraint [24]. Based on the SEM–EDS mapping of Al and Si in Fig. 4d1 and d2, the melt pool boundary is richer in the Si element. The formation of large discrete Si particles at melt pool boundaries has also been observed for the WAAM-processed 4043 aluminum alloys [14]. In contrast, α-Al and faceted Si phases are solidified in a coupled growth mode and form relatively regular eutectic morphologies within melt pools. The average length of eutectic Si in the AM300 and AM420 alloys is 0.8 µm and 0.5 µm, respectively, lower than that of the cast alloy (1.9 µm). This indicates the refinement of Si particle enabled by WAAM, and an additional refinement can be obtained by a higher travel speed of welding torch.

Besides α-Al and eutectic Si phases, sub-micron Fe-rich intermetallic compounds in bright-contrast are also observed in AM300 (averaged 0.5 µm in length) and AM420 alloys (averaged 0.9 µm in length), mainly at the interfaces between α-Al dendrites and eutectics (Fig. 4 a3 and b3). For comparison, the coarse needle-like Fe-rich intermetallic compounds,
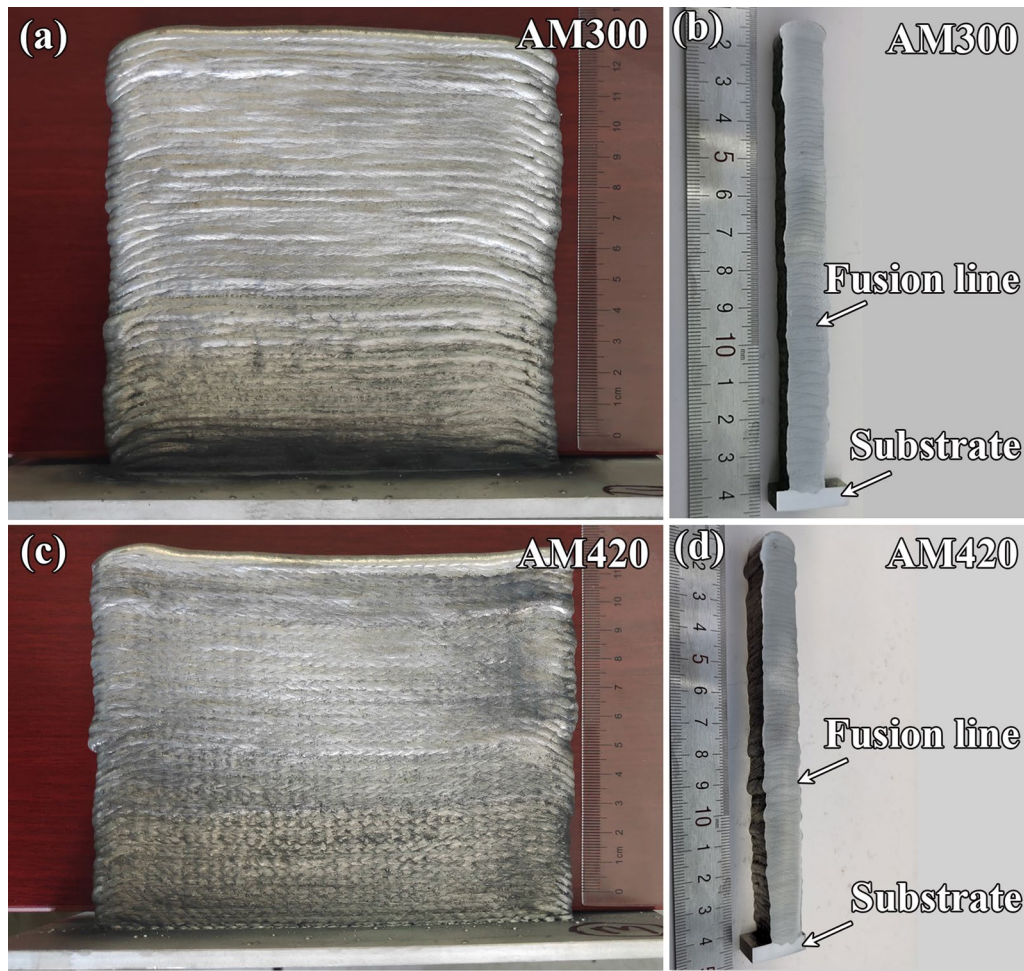
Fig. 2 Front **a**, **c** and sectional **b**, **d** views of conventional WAAM-fabricated 4047 Al–Si alloys with a respective travel speed of 300 mm/min (AM300, **a**, **b**) and 420 mm/min (AM420, **c**, **d**)

averaged 5.7 μm in length, are produced in the interdendritic regions (Fig. 4 c3). Besides, Fe-rich intermetallic compounds are more dispersive in the WAAM-processed alloys than that in the cast counterpart alloy. Namely, both nucleation position and growth rate of the Fe-rich intermetallic compounds are affected by the rapid solidification process of WAAM, and significant refinement can be achieved.

3.2 Porosity Characterization

Metallurgical defects are often fatal to engineering aluminum materials, especially porosity. With this consideration, we investigate the three-dimensional geometry and distribution of pores within the WAAM-processed AM300 and AM420 alloys. The reconstructions of pores are shown in Fig. 5, and most pores display spherical morphologies, suggesting the dominance of gas pores with negligible shrinkage cavities formed during WAAM processing. The volume fraction of gas pores is 1.1% for the AM300 alloy and 1.2%

for the AM420 alloy. It manifests, in this work, the welding torch travel speed produces a limited effect on the volume fraction of hydrogen pores for the WAAM-processed Al–Si alloys. Noteworthily, hydrogen pores are also found in cast counterpart alloy, and the corresponding volume fraction is ~0.6%, measured from the optical microstructure images.

Statistical porosity analysis is then performed to interpret the effect of welding torch travel speed on the porosity for WAAM-processed Al–Si alloys. Figure 6 shows the pores' relative frequencies of aspect ratio and Feret diameter, i.e., maximum distance between two points on the surface. The closer the aspect ratio to 1, the higher sphericity of the pore. The highest relative frequency of the aspect ratio for AM300 and AM420 alloys is 0.80–0.85 and 0.70–0.75, respectively (Fig. 6a, c). The mean Ferret diameter of the three alloys is below 110 μm, as shown in Fig. 6b, d. The highest relative frequency of mean Ferret diameter is 27.3% for the AM300 alloy in the range of 20–30 μm, and 45.2% for the AM420 alloy in the range of 10–20 μm. Above results reveal that a

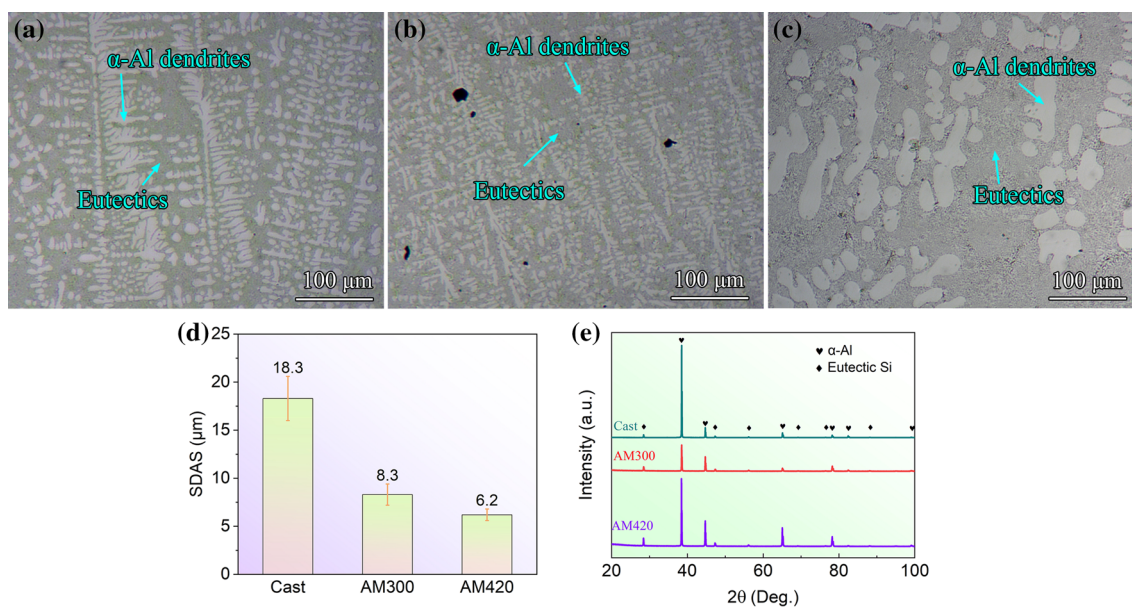**Fig. 3** Optical images of the microstructures within melt pools for WAAM-fabricated 4047 Al–Si alloys with a respective travel speed of 300 mm/min (AM300, **a** and 420 mm/min (AM420, **b**), as well as the cast counterpart alloy **c**. **d** Secondary dendrite arm spacing (SADS) of each alloy. **e** XRD spectra of conventional cast alloy as well as AM300 and AM420 alloys

higher travel speed of welding torch leads to a reduced pore sphericity and a lower pore diameter for Al–Si alloys via WAAM. It suggests increasing the solidification rate promotes the gas pore nucleation and suppresses its growth.

3.3 Mechanical Property

The tensile properties of experimental Al–Si alloys are tabulated in Table 2. The average yield strength (YS) and ultimate tensile strength (UTS) of the cast alloy are 88.3 MPa and 173.1 MPa, respectively, with an average elongation after fracture of 17.8%. The AM300 and AM420 alloys show a negligible strength anisotropy, with comparable YS and UTS values along SD and BD. The AM420 alloy shows a higher strength, including both YS and UTS, and a lower elongation than the AM300 alloy along both SD and BD. Compared with the cast Al–Si alloy, the WAAM-processed alloys achieve higher YS (up to 98.0 MPa) and UTS (up to ~206.4 MPa), respectively, with a lower elongation after fracture between 14.4 and 10.6%. The UTS and YS values of the 4047 Al–Si alloy fabricated via gas metal arc welding (GMAW)-based WAAM are ~192 MPa and 88 MPa, respectively, both of which are lower than the alloy processed by the CMT-based WAAM method in this work [19].

The fracture surfaces after tensile testing are displayed in Fig. 7, with evident fractured pores. Both dimple and cleavage fracture modes are observed. Combined with EDS scanning of the selected region that shows Al and Si distributions, α-Al dendrites are fractured in a cleavage mode, while interdendritic eutectics in a dimple mode. Figure 8

shows the fracture surfaces of the cast Al–Si alloy counterpart, and still, several pores are found. α-Al dendrites and interdendritic eutectics are distinguished by the distributions of Al and Si (Fig. 8d, e). The former is fractured in a cleavage mode, and the latter is fractured in a dimple mode, which is in accordance with that for WAAM-processed alloys. An extra finding is the observation of Fe-rich phases on the fracture surfaces (Fig. 8c, f), which, however, are not found on the fracture surfaces of WAAM-processed Al–Si alloys.

4 Discussion

Figure 9 summarizes the effects of WAAM on the microstructure, porosity and mechanical property of Al–Si alloys, obtained by comparing the AM420 alloy and the cast counterpart alloy. Significant microstructure refinement is enabled via WAAM, including SDAS, eutectic Si particle length and Fe-rich intermetallic compound size. The corresponding refinement mechanisms can be threefold, including rapid solidification correlated with fast traveling of welding torch and large temperature gradient, agitating effect of arc on melt pool to break dendrite arms and facilitate heterogeneous nucleation, and the improved nucleation sites due to its layer-wise fabrication [2, 3, 8, 14]. In addition, the Al–Si alloy melt possibly experiences a large superheating, which also contributes to microstructural refinement [25, 26].

A larger travel speed of welding torch, from 300 to 420 mm/min, corresponds to a further microstructure refinement, which is associated with the reduced heat input
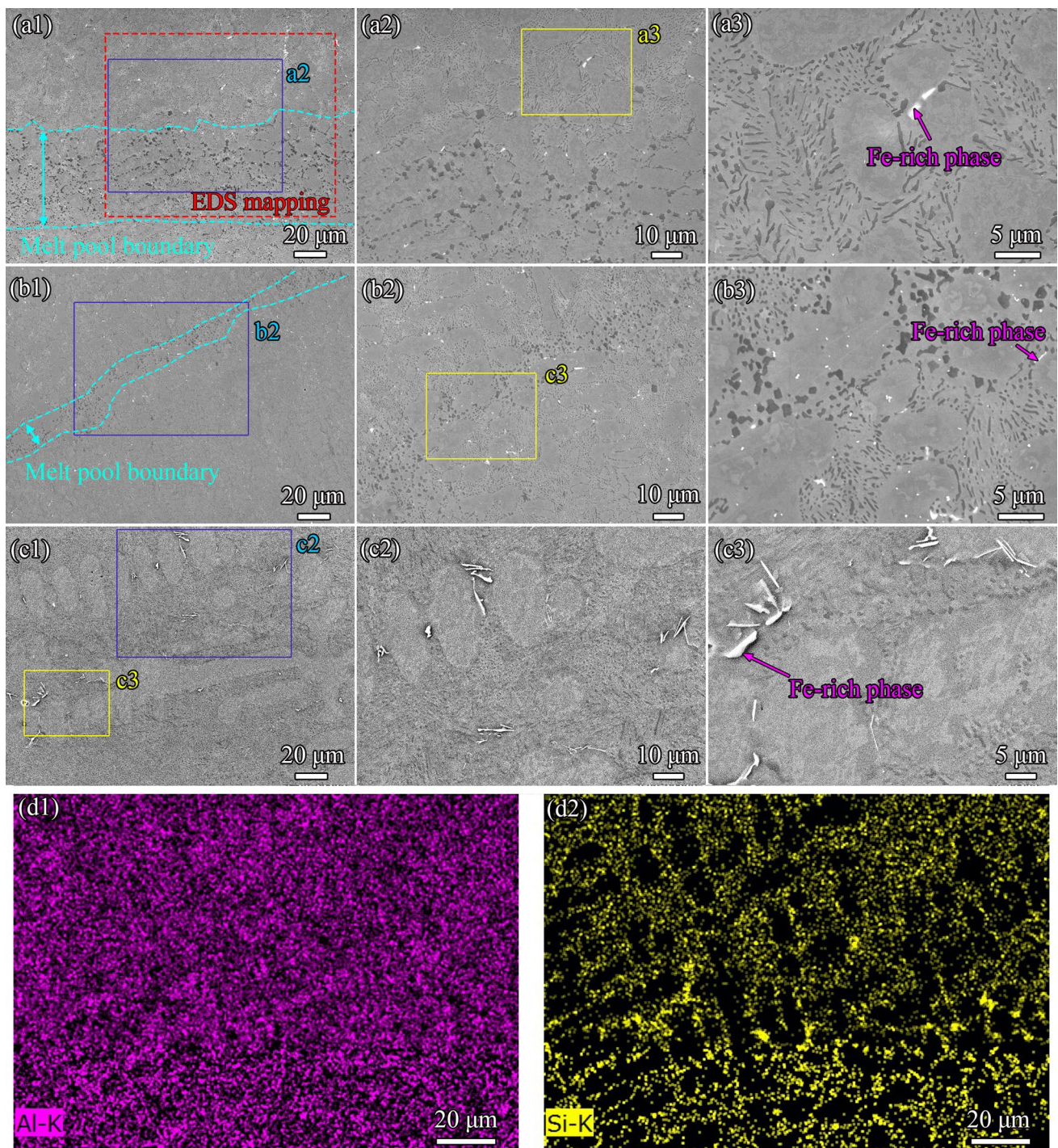
Fig. 4 SEM images showing the microstructures at melt pool boundaries for WAAM-fabricated 4047 Al–Si alloys with a respective travel speed of 300 mm/min (AM300, **a**1, **a**2, **a**3) and 420 mm/min (AM420, **b**1, **b**2, **b**3), as well as the cast counterpart alloy **c**1, **c**2, **c**3. **d**1 and **d**2 SEM–EDS mapping of Al and Si within the selected region shown in **a**1

and the increased solidification rate [17, 27]. Meanwhile, the maximum temperature within the melt pool is reduced by increasing travel speed [28], forming a thinner melt pool boundary (Fig. 4).

Such a microstructural modification arising from WAAM produces a positive effect on the mechanical properties including both YS and UTS. The strengthening effect provided by grain refinement has been well established
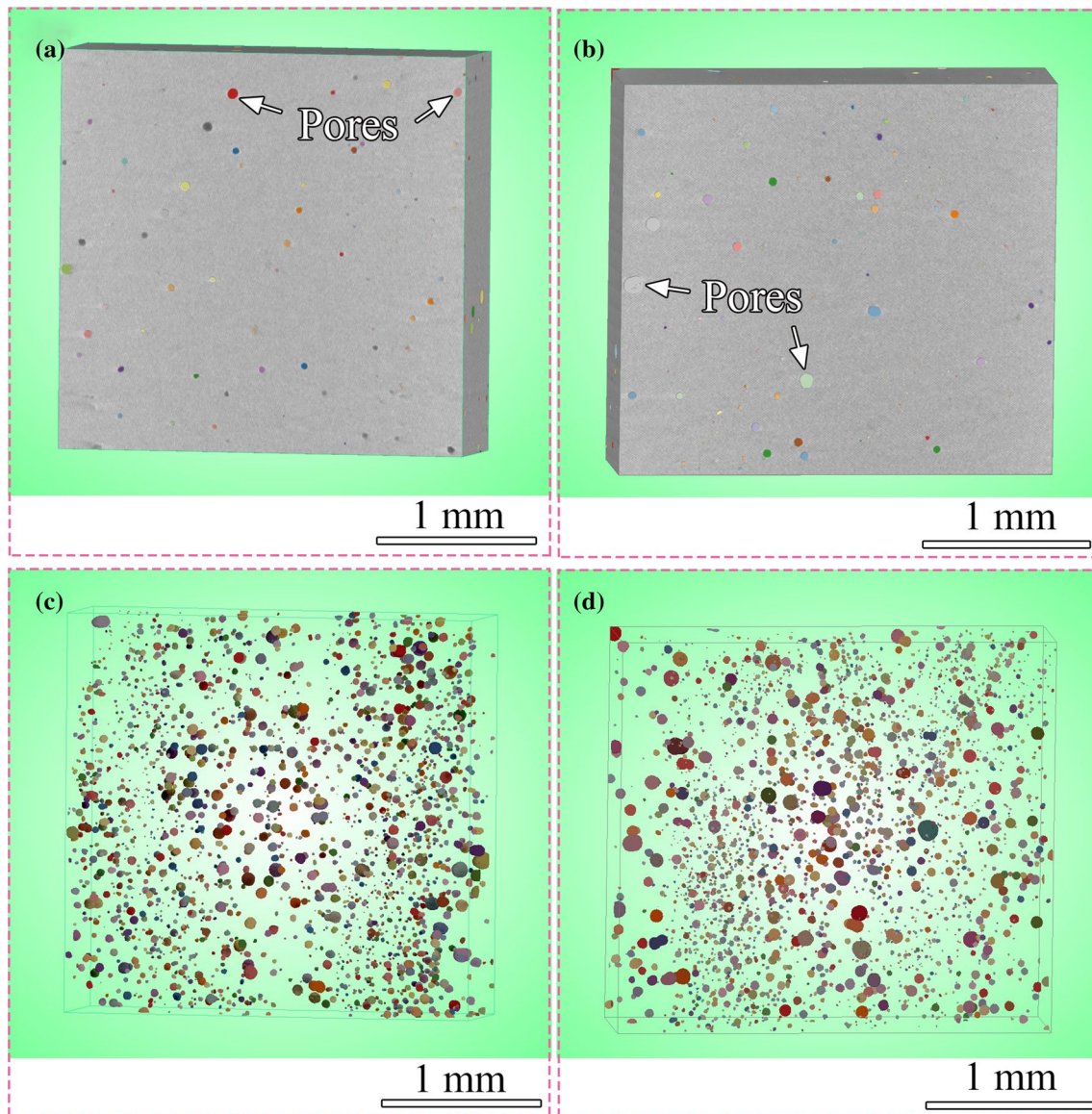
Fig. 5 Three-dimensional distributions of pores within the WAAM-fabricated 4047 Al–Si alloys with a respective travel speed of 300 mm/min (AM300, **a**, **c**) and 420 mm/min (AM420, **b**, **d**). The gray-contrast background in **a** and **b** is the alloy sample. **c**, **d** Pores extracted from **a**, **b**, respectively, with colored surfaces

for wrought polycrystalline alloys, following the classical Hall–Petch equation, i.e., a linear relationship between flow stress and inverse square root of the grain size (Eq. 1) [29, 30]:

$$\sigma = \sigma_0 + \frac{k}{\sqrt{d}} \tag{1}$$

where σ_0 and k are constants, and d represents the grain size. To modify the Hall–Petch equation for Al–Si alloys with complex two-phase microstructures, SDAS is used to replace grain size, and near-linear laws are found between UTS/YS and inverse square root of SDAS [31]. Dendrite boundaries

are the obstacles to resist dislocation movement, resulting in an effective strength increase [29, 30]. This explains the improvement of YS and UTS mediated by a faster travel speed of welding torch in our work. The hard eutectic Si particles are effective strengthening phases for Al–Si alloys, and the corresponding dispersion strengthening can be further improved by size reduction [32]. The decrease in melt pool boundary width can provide additional improvements in UTS and YS, as the large bulk Si particles in melt pool boundary tend to break more easily and thus deteriorate alloys' strength [14].

Fe-rich intermetallic compounds are the notorious harmful phases for Al–Si alloys that often cause stress
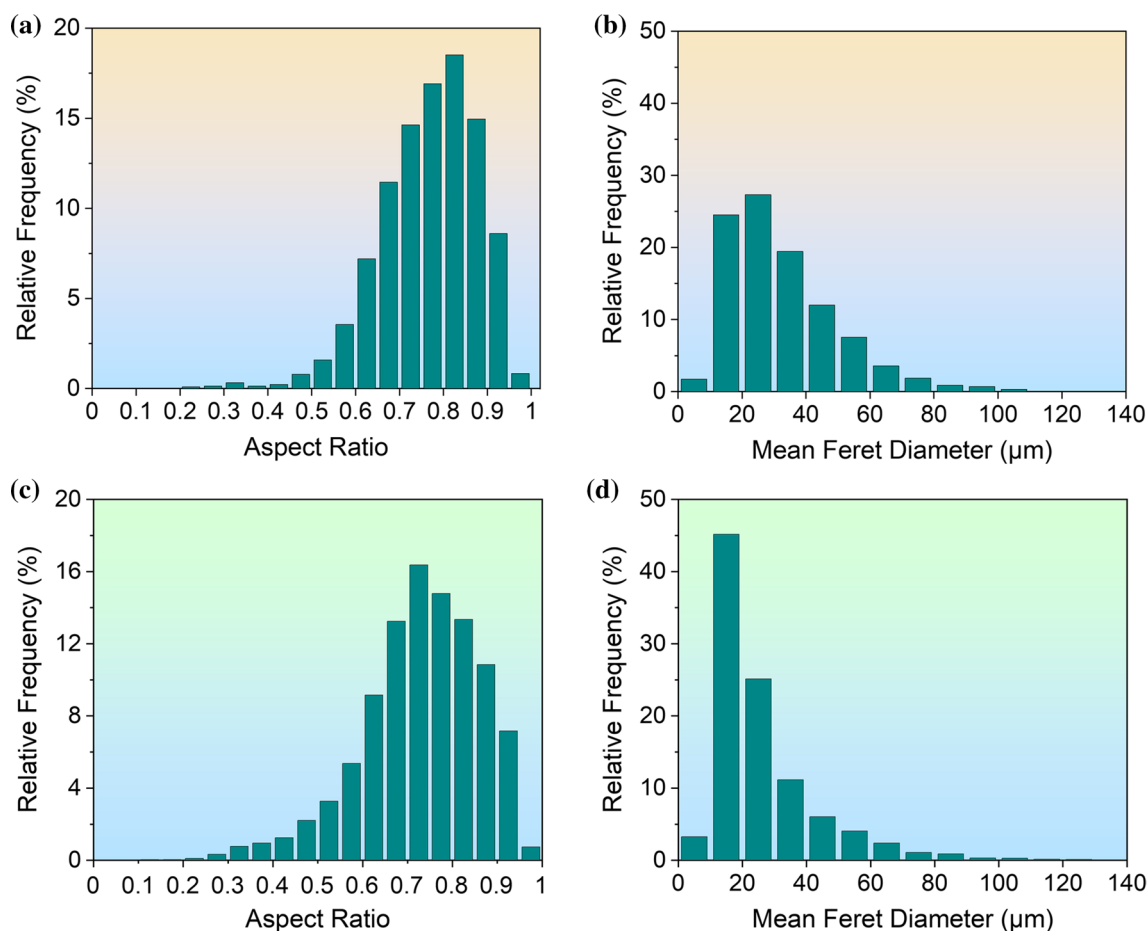
Fig. 6 Relative frequencies of aspect ratio and mean Feret diameter for the WAAM-fabricated 4047 Al–Si alloys with a respective travel speed of 300 mm/min (AM300, **a**, **c**) and 420 mm/min (AM420, **b**, **d**)

Table 2 Mechanical properties of cast and WAAM-fabricated Al–Si alloys using SAL4047 welding wires with travel speeds of 300 mm/min (AM300) and 420 mm/min (AM420)

Alloys	Yield strength (MPa)	Ultimate tensile strength (MPa)	Elongation after fracture (%)
Cast	88.3 ± 1.6	173.1 ± 2.4	17.8 ± 4.3
AM300-SD	92.3 ± 0.7	196.7 ± 0.8	14.4 ± 0.1
AM300-BD	92.2 ± 3.0	193.4 ± 3.5	11.6 ± 1.5
AM420-SD	98.0 ± 3.1	204.5 ± 5.1	13.2 ± 0.1
AM420-BD	96.6 ± 0.5	205.6 ± 5.8	10.6 ± 1.1

Sampling from scanning direction (SD) and building direction (BD) is performed for mechanical testing, respectively, as illustrated in Fig. 1b

concentration under mechanical loading, acting as crack initiation sites caused by their larger elastic modulus [10, 33]. It is also evidenced in this work with the presence of Fe-rich phases on the fracture surface of cast Al–Si alloys (Fig. 8). The agglomerated Fe-rich intermetallic compounds in needle-like morphologies are suppressed, and instead, refined dispersive compounds are obtained via WAAM, which contributes to the improvement of mechanical property of Al–Si alloys. Additional strengthening can also be provided by such refined dispersive Fe-rich compounds [34]. Therefore, WAAM can be considered as a promising pathway to solve the headache issue of harmful Fe-rich intermetallic compounds.

Negative effects on porosity and elongation after fracture are caused by WAAM processing, as red-colored in Fig. 9. Al–Si alloys fabricated by WAAM suffer from severer defects of gas porosity than the cast alloy with the higher volume fraction increasing from 0.6 to 1.2%. This finding is in accordance with the results observed by Ma et al [35]. The gas porosity is mainly caused by the rapidly decreased hydrogen solubility in aluminum during liquid→solid transformations and thus the formation of supersaturated hydrogen [36]. During WAAM, the unfavorable hydrogen primarily comes from wire surface contaminants, atmosphere and shielding gases, etc., and therefore is less controllable in comparison with conventional casting [8,
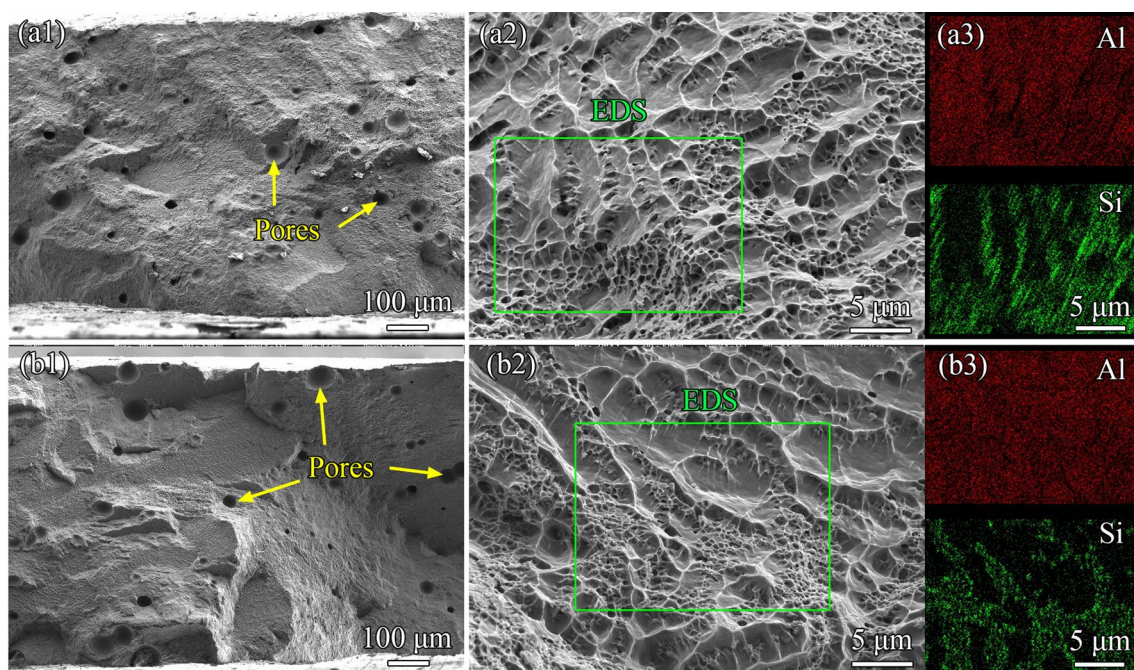
Fig. 7 Fracture surfaces of the WAAM-fabricated 4047 Al–Si alloys with a respective travel speed of 300 mm/min (AM300-SD, **a**, **c**) and 420 mm/min (AM420-SD, **b**, **d**). **a**3 and **b**3 SEM–EDS mapping of the selected region in **a**2 and **b**2, respectively, showing the distributions of Al and Si
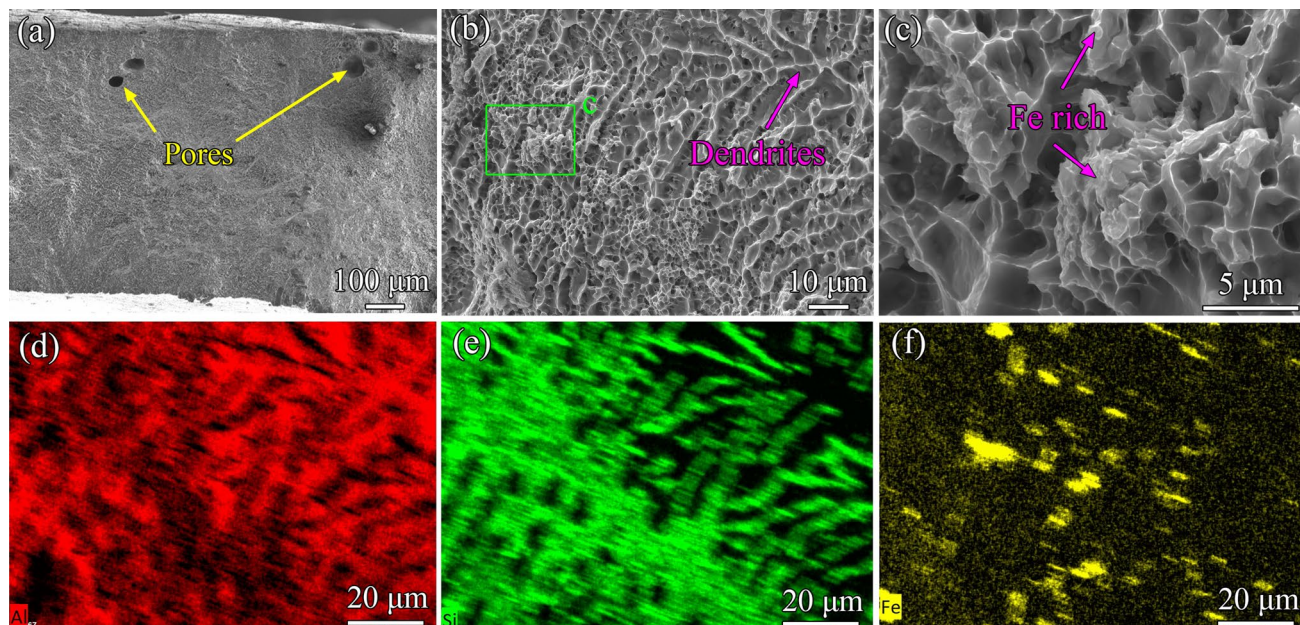

Fig. 8 Fracture surface of the cast counterpart 4047 Al–Si alloy **a–c** and the corresponding SEM–EDS mapping of the distributions of Al **d**, Si **e** and Fe **f**, respectively

11, 37, 38]. Porosity is known to greatly affect aluminum alloy's mechanical property, especially ductility [39–41]. According to the observation of in situ tensile testing, large pores are elongated along the loading direction, displaying a higher tendency for crack initiation and bridging in the

WAAM-processed 205A aluminum alloys, which is closely correlated with the deteriorated ductility [35]. The presence of gas pores could reduce the actual bearing area and facilitate stress concentration at pore edges, which explains the lower elongation after fracture of the WAAM-processed
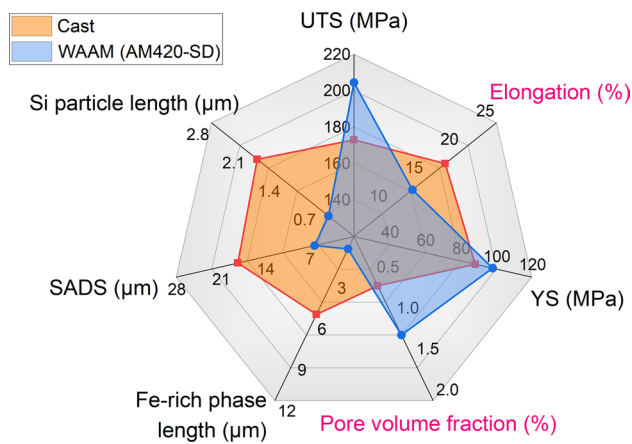
Fig. 9 Radar chart to compare the porosity, microstructure and mechanical property of 4047 Al–Si alloys via WAAM and conventional casting

alloys than the cast alloy. With a higher travel speed of welding torch during WAAM, both size and sphericity of pores are reduced, as a result of a higher solidification rate (Fig. 6). Decreasing the sphericity of pores can increase the tendency of stress concentration in the AM420 alloy [35, 42], and resultantly, the elongation after fracture decreases in comparison with the AM300 alloy.

Based on the above comparative study, we can gain the knowledge that in addition to the well-known fabrication advantages, WAAM enables a strength improvement for the 4047 Al–Si alloys, with a decreased (but acceptable) ductility, in comparison with conventional casting. The previous literature has reported that property anisotropy is obvious for Al–Cu and Al–Zn–Cu–Mg alloys via WAAM [43, 44] as well as other additive manufacturing methods [45, 46]. This property anisotropy is caused by two main factors. On the one side, alternating equiaxed and columnar grains are formed in each deposition layer, leading to the grain size diversity along different directions; on the other sides, the anisotropic diameter and volume fraction of interlayer pores result in a distinct response to mechanical loading [43–46]. However, negligible property anisotropy for Al–Si alloys via WAAM is found in this work owing to the relatively isotropous microstructure and homogeneous spatial distribution of pores, which is of importance for engineering applications.

5 Conclusions

This work has investigated the microstructure, porosity and mechanical property of 4047 Al–Si alloys fabricated by WAAM and conventional casting. Our findings are concluded as follows.

1. Primary α-Al dendrites are formed in the experimental alloys, and the melt pool boundaries are featured by large bulk Si particles. Compared with conventional casting, significant microstructure modifications are achieved by WAAM, i.e., refinements of SDAS, eutectic Si and Fe-rich compound length. Microstructure refinement is further promoted by applying a higher travel speed of welding torch.

2. A higher volume fraction of gas pores up to 1.2%, with a high sphericity close to 1 are generated during WAAM, in comparison with conventional casting (0.6%). A limited effect on pore fraction is caused by increasing the travel speed from 300 to 420 mm/min.

3. Higher strengths and lower elongations after fracture are obtained in WAAM-processed alloys compared to the cast alloy, with the UTS up to ~205.6 MPa and the YS up to ~98.0 MPa. Further improvement in UTS and YS is achieved by applying a higher travel speed of welding torch from 300 mm/min to 420 mm/min. Negligible mechanical property anisotropy along scanning and building directions is found for Al–Si alloys via WAAM.

References

[1] M. Köhler, S. Fiebig, J. Hensel, K. Dilger, Metals **9**, 608 (2019)

[2] Y. Zhou, X. Lin, N. Kang, W. Huang, J. Wang, Z. Wang, J. Mater. Sci. Technol. **37**, 143 (2020)

[3] R. Fu, S. Tang, J. Lu, Y. Cui, Z. Li, H. Zhang, T. Xu, Z. Chen, C. Liu, Mater. Des. **199**, 109370 (2021)

[4] J.L. Gu, J.L. Ding, B.Q. Cong, J. Bai, H.M. Gu, S.W. Williams, Y.C. Zhai, Adv. Mater. Res. **1081**, 210 (2014)

[5] H. Li, J. Zou, J. Yao, H. Peng, J. Alloys Compd. **727**, 531 (2017)

[6] B. Cong, Z. Qi, B. Qi, H. Sun, G. Zhao, J. Ding, Appl. Sci. **7**, 275 (2017)

[7] D. Zhang, G. Wang, A. Wu, J. Shan, Y. Zhao, T. Zhao, D. Meng, J. Song, Z. Zhang, Acta Metall. Sin. Engl. Lett. **32**, 684 (2019)

[8] D. Wang, J. Lu, S. Tang, L. Yu, H. Fan, L. Ji, C. Liu, Materials **11**, 1344 (2018)

[9] T. Lu, C. Liu, Z. Li, Q. Wu, J. Wang, T. Xu, J. Liu, H. Wang, S. Ma, J. Alloys Compd. **817**, 153334 (2020)

[10] Z. Li, N. Limodin, A. Tandjaoui, P. Quaegebeur, J. Witz, D. Balloy, Mater. Sci. Eng. A **794**, 139920 (2020)

[11] B. Cong, J. Ding, S. Williams, Int. J. Adv. Manuf. Technol. **76**, 1593 (2015)

[12] O. Panchenko, D. Kurushkin, I. Mushnikov, A. Khismatullin, A. Popovich, Mater. Des. **195**, 109040 (2020)

[13] A. Elrefaey, N.G. Ross, Acta Metall. Sin. -Engl. Lett. **28**, 715 (2015)

[14] Q. Miao, D. Wu, D. Chai, Y. Zhan, G. Bi, F. Niu, G. Ma, Mater. Des. **186**, 108205 (2020)

[15] B. Dong, X. Cai, S. Lin, X. Li, C. Fan, C. Yang, H. Sun, Addit. Manuf. **36**, 101447 (2020)

[16] Z. Qi, B. Cong, B. Qi, H. Sun, G. Zhao, J. Ding, J. Mater. Process. Technol. **255**, 347 (2018)

[17] C. Su, X. Chen, C. Gao, Y. Wang, Appl. Surf. Sci. **486**, 431 (2019)

[18] Q. Yang, C. Xia, Y. Deng, X. Li, H. Wang, Materials **12**, 432 (2019)

[19] A.S. Haselhuhn, M.W. Buhr, B. Wijnen, P.G. Sanders, J.M. Pearce, Mater. Sci. Eng. A **673**, 511 (2016)

[20] T.A. Mai, A.C. Spowage, Mater. Sci. Eng. A **374**, 224 (2004)

[21] J.L. Murray, A.J. McAlister, Bull. Alloy Phase Diagrams **5**, 74 (1984)

[22] Y. Zhao, Y. Jia, S. Chen, J. Shi, F. Li, Addit. Manuf. **32**, 100935 (2020)

[23] Y. Guo, L. Jia, S. Sun, B. Kong, J. Liu, H. Zhang, Mater. Des. **109**, 37 (2016)

[24] A.J. Shahani, X. Xiao, P.W. Voorhees, Nat. Commun. **7**, 12953 (2016)

[25] J. Wang, S. He, B. Sun, Q. Guo, M. Nishio, J. Mater. Process. Technol. **141**, 29 (2003)

[26] X.P. Li, X.J. Wang, M. Saunders, A. Suvorova, L.C. Zhang, Y.J. Liu, M.H. Fang, Z.H. Huang, T.B. Sercombe, Acta Mater. **95**, 74 (2015)

[27] L. Huang, X. Chen, S. Konovalov, A.N. Siddiquee, G. Lu, X. Pan, Metals **11**, 267 (2021)

[28] T. Mukherjee, V. Manvatkar, A. De, T. DebRoy, Scr. Mater. **127**, 79 (2017)

[29] S. Najafi, A.R. Eivani, M. Samaee, H.R. Jafarian, J. Zhou, Mater. Charact. **136**, 60 (2018)

[30] W. Xu, L.P. Dávila, Mater. Sci. Eng. A **710**, 413 (2018)

[31] E. Ghassemali, M. Riestra, T. Bogdanoff, B.S. Kumar, S. Seifeddine, Procedia Eng. **207**, 19 (2017)

[32] H. Lien, J. Mazumder, J. Wang, A. Misra, Mater. Res. Lett. **8**, 291 (2020)

[33] L. Kucharíková, M. Mazur, E. Tillová, M. Chalupová, D. Závodská, A. Vaško, Eng. Failure Anal. **105**, 688 (2019)

[34] H. Li, B. Lin, R. Xu, K. Liu, H. Xiao, Y. Zhao, Mater. Sci. Technol. **36**, 307 (2020)

[35] T. Ma, J. Ge, Y. Chen, T. Jin, Y. Lei, Mater. Lett. **237**, 266 (2019)

[36] A.P. Boeira, I.L. Ferreira, A. Garcia, Mater. Des. **30**, 2090 (2009)

[37] J. Gu, J. Ding, S.W. Williams, H. Gu, P. Ma, Y. Zhai, J. Mater. Process. Technol. **230**, 26 (2016)

[38] E.M. Ryan, T.J. Sabin, J.F. Watts, M.J. Whiting, J. Mater. Process. Technol. **262**, 577 (2018)

[39] J. Rao, J. Zhang, R. Liu, J. Zheng, D. Yin, Mater. Sci. Eng. A **728**, 72 (2018)

[40] S. Dezecot, V. Maurel, J. Buffiere, F. Szmytka, A. Koster, Acta Mater. **123**, 24 (2017)

[41] G. Liu, J. Xiong, L. Tang, Addit. Manuf. **35**, 101375 (2020)

[42] E. Lordan, J. Lazaro-Nebreda, Y. Zhang, K. Dou, P. Blake, Z. Fan, Mater. Sci. Eng. A **778**, 139107 (2020)

[43] Z. Yu, T. Yuan, M. Xu, H. Zhang, X. Jiang, S. Chen, J. Manuf. Process. **62**, 430 (2021)

[44] Z. Qi, B. Qi, B. Cong, H. Sun, G. Zhao, J. Ding, J. Manuf. Process. **40**, 27 (2019)

[45] Q. Tan, J. Zhang, Q. Sun, Z. Fan, G. Li, Y. Yin, Y. Liu, M. Zhang, Acta Mater. **196**, 1 (2020)

[46] J.H. Martin, B.D. Yahata, J.M. Hundley, J.A. Mayer, T.A. Schaedler, T.M. Pollock, Nature **549**, 365 (2017)